Synthesis of 3D Hierarchical Self Assembled Microstructures Formed from alpha MnO2 Nanotubes and Their Conducting and Magnetic Properties

12 AUTHORS, INCLUDING:

Polona Umek
Jožef Stefan Institute
81 PUBLICATIONS   1,076 CITATIONS
SEE PROFILE

Alexandre Gloter
Université Paris-Sud 11
120 PUBLICATIONS   3,717 CITATIONS
SEE PROFILE

Anton Potočnik
Jožef Stefan Institute
25 PUBLICATIONS   379 CITATIONS
SEE PROFILE

Denis Arcon
Jožef Stefan Institute
221 PUBLICATIONS   2,486 CITATIONS
SEE PROFILE

Synthesis of 3D Hierarchical Self-Assembled Microstructures Formed from α-MnO₂ Nanotubes and Their Conducting and Magnetic Properties

Polona Umek,*,† Alexandre Gloter,‡ Matej Pregelj,† Robert Dominko,§ Marko Jagodič,‖ Zvonko Jagličić,‖,⊥ Anna Zimina,# Mery Brzhezinskaya,#,▽ Anton Potočnik,† Cene Filipič,† Adrijan Levstik,† and Denis Arčon†,○

Jožef Stefan Institute, Jamova 39, Ljubljana, Slovenia, Laboratoire de Physique des Solides, CNRS UMR8502, Université Paris Sud, Orsay, France, Nacional Institute of Chemistry, Hajdrihova 19, Ljubljana, Slovenia, Institut of Mathematics, Physics and Mechanics, Jadranska 19, Ljubljana, Slovenia, Faculty of Civil and Geodetic Engineering, University of Ljubljana, Jamova 2, Ljubljana, Slovenia, BESSY m.b.H., Albert-Einstein-Strasse 15, Berlin, Germany, V.A. Fock Institute of Physics, St. Petersburg State University, St. Petersburg, Russia, Faculty for Mathematics and Physics, University of Ljubljana, Jadranska 19, Ljubljana, Slovenia

Highly crystalline α-MnO₂ nanotubes with outer diameters between 25 and 40 nm are formed by a hydrothermal decomposition of $KMnO_4$ precursor in an acidic environment. For nanotube formation, it is essential to include an addition of Fe^{3+} ions in the reaction mixture. SEM and TEM studies reveal that nanotubes are self-assembled into three-dimensional hollow microstructures where the shell thickness corresponds to the average nanotube length (~370 nm). The intercalation of K^+ and Fe^{3+} ions into the α-MnO₂ structure determines the local Mn^{3+}/Mn^{4+} ratio, and with this, influences their electric conductivity and magnetic properties. At high temperatures, the small polaron hopping of the e_g electron from a Jahn−Teller-active Mn^{3+} ($t_{2g}^3 e_g^1$) to a non-active Mn^{4+} ($t_{2g}^3 e_g^0$) site is responsible for the activated type of conductivity in mixed Mn^{3+}/Mn^{4+} regions with the activation energy $E_a/k_B = 2200$ K. Magnetic susceptibility and EPR measurements show two distinct behaviors, suggesting nanometric phase segregation into mixed Mn^{3+}/Mn^{4+} and nearly pure Mn^{4+} regions. At low temperatures, an antiferromagnetic ordering occurs at $T_N = 13.6$ K, which is substantially lower than in bulk α-MnO₂ phases.

Introduction

The self-assembly of nanoparticles into two- (2D) or three-dimensional (3D) structural architectures is driven by the weak interactions (van der Waals or hydrogen bonds) between building blocks. This offers exciting possibilities for tailoring and tuning of chemical and physical properties of materials and expands their range of functional properties.[1−3] For instance, the self-assemblies of complex nanostructures with an increased number of active sites[4,5] may show significantly improved sensing or catalytic activity on account of their thermodynamic stability. The self-assembly process is also an important strategy in the nanofabrication of architectures built from magnetic nanoparticles for which precise control over the nanoparticle magnetic state and the magnetic interactions between the particles is required. Up to now, different manganese oxide nanoparticles have been intensely investigated in connection with their adsorption and magnetic properties, but their self-assemblies are scarcely reported.

MnO_2 exists in several polymorphic forms,[6] which are efficient in a wide range of technological applications, such as cathode material in alkaline and rechargeable batteries,[6−8] molecular sieves,[9] catalysis,[10] and magnetic applications.[11] Chemical and physical properties of MnO_2 phases that stem from the redox flexibility of manganese ions found in oxidation states 4+ and 3+ also strongly depend on their structure and morphology.[12] Lately, much research effort has been directed toward synthesis of nanosized MnO_2 of different morphologies.[13−17] Most of the reaction pathways lead to particles in the shape of nanorods. However, reports on MnO_2 nanotubes (NTs), the most desirable morphology, are very limited thus far.[18−22]

Here, we report for the first time on the synthesis of α-MnO₂ NTs that are self-assembled into unique 3D hollow microspheres at a scale of a few micrometers. The length of individual NTs is on average ~370 nm, whereas their diameters are found to be between 25 and 40 nm. The effect of ordering at different scales on the transport and magnetic properties has also been studied. Investigated self-assembly structures show nanoscale inhomogeneities that depend on the presence of Mn^{3+} ions in the Mn^{4+} lattice dictated by small variations in the chemical composition. This property may be common to many manganese oxide nanoparticle self-assemblies and has to be taken into account for their future applications.

Experimental Section

Synthesis. In a typical experimental procedure, 1.6 mmol of $KMnO_4$ and 0.12 mmol of $Fe_2(SO_4)_3$ were dissolved in 18 mL of distilled water to form a homogeneous solution. After the addition of 0.8 mL of concentrated H_2SO_4, the reaction mixture was loaded into a 23 mL, Teflon-lined, stainless steel autoclave.

* Corresponding author. Phone: +386-1-4773-500. Fax: +386-1-4773-191. E-mail: polona.umek@ijs.si.
† Jožef Stefan Institute.
‡ Université Paris Sud.
§ Nacional Institute of Chemistry.
‖ Institut of Mathematics, Physics and Mechanics.
⊥ Faculty of Civil and Geodetic Engineering, University of Ljubljana.
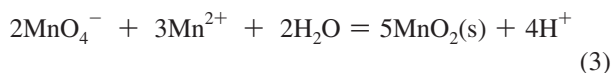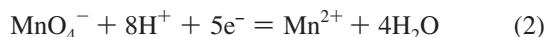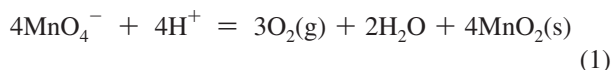# BESSY m.b.H.
▽ St. Petersburg State University.
○ Faculty for Mathematics and Physics, University of Ljubljana.

The autoclave was sealed and heated in an oven at 150 °C for 17 h. When cooled to room temperature, a resulting brown-black precipitate was collected by centrifugation; washed with 30 mL of distilled water; and finally, dried at 100 °C overnight.

Characterization Techniques. XRD patterns were preformed with a PANalytical X'Pert PRO high-resolution diffractometer with Cu K$_{\alpha 1}$ radiation (1.5406 Å). The morphology of the synthesized product was investigated with filed emission SEM (Carl Zeiss, Supra 35LV equipped) and TEM (Jeol 2100, 200 keV). The scanning transmission electron spectroscopy (STEM)−HAADF and STEM−energy loss spectroscopy (EELS) measurements were preformed with a dedicated STEM (Vacuum Generators HB 501) equipped with a home-modified Gatan spectrometer. All spectra were recorded in STEM mode with 100 keV incident electrons focused on the specimen. EELS mapping was obtained by rastering a 1 nm probe on the surface of the single nanotube and collecting spectra with a spectral domain from 200 to 900 eV. Local compositions were then obtained by extractions of O 1s, Mn 2p, and Fe 2p excitations. SXA in a total electron yield mode with an energy resolution of 100 at the Mn 2p absorption edge were measured at the Russian−German beamline at BESSY II (Germany).[23] For the measurements, the powdered samples were pressed into In foil. Magnetic susceptibility between 2 and 300 K and magnetization curves up to 5 T were measured with a Quantum Design MPMS XL-5 SQUID magnetometer. X-band EPR measurements were preformed on a commercial Bruker E580 spectrometer equipped with an Oxford Cryogenics ESR900 cryostat. Electrical transport properties were measured using a home-made extension for the Quantum Design MPMS XL-5 system having the sample temperature and magnetic field measuring intervals as for magnetic measurements. Electrical conductivity of the product in the form of a pressed pellet was measured as a function of temperature and magnetic field with the standard four-contacts technique.

Results and Discussion

At elevated temperatures, an acidic solution of KMnO$_4$(aq) is reduced to MnO$_2$ by two different reaction pathways:[24] (i) Permanganate solution is intrinsically unstable, and it decomposes according to reaction 1. Reaction itself proceeds faster in an acidic environment. (ii) Following the second pathway, an acidic solution of permanganate is first reduced to Mn^{2+}(aq) (reaction 2), and in the second step, excess MnO$_4^-$(aq) oxidizes Mn^{2+}(aq) (reaction 3), which yields MnO$_2$.

$$4MnO_4^- + 4H^+ = 3O_2(g) + 2H_2O + 4MnO_2(s) \tag{1}$$

$$MnO_4^- + 8H^+ + 5e^- = Mn^{2+} + 4H_2O \tag{2}$$

$$2MnO_4^- + 3Mn^{2+} + 2H_2O = 5MnO_2(s) + 4H^+ \tag{3}$$

In our case, the reaction mixture was slightly modified by the addition of Fe^{3+}(aq) ions. Their presence in the reaction mixture stimulated the growth of MnO$_2$ nanotubes over nanorods,[25−27] and under the applied conditions, Fe^{3+}(aq) ions did not react with either MnO$_4^-$(aq) or Mn$_2^+$(aq).

The morphology of an isolated product was first examined with a scanning electron microscope (SEM). The product is on a larger scale composed of hollow microspheres, as shown in
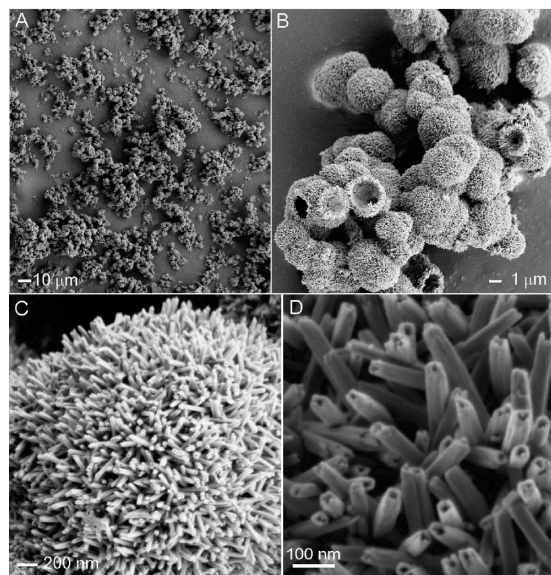
Figure 1. FE-SEM images of α-MnO$_2$-based product doped with Fe^{3+}: (a) a panoramic view at small magnification, (b) a conglomerate of microspheres, (c) an individual microsphere with a typical diameter of 3 μm and (d) top-view on the microsphere shell that is composed of compactly arranged NTs. The microspheres are hollow (image b), and the shell thickness agrees well with the length of individual NTs. Tetragonal cavities of NTs can be clearly observed from image d.
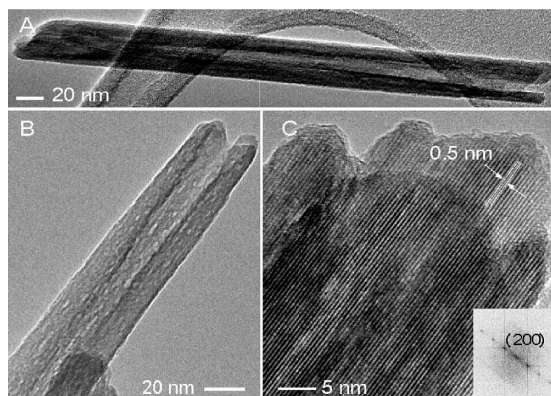
Figure 2. TEM images of MnO$_2$ NT (a) and NT ends (b and c). From images a and b, one can observe that the inner diameter gradually reduces with the distance from the NT end.

the SEM images (Figure 1a and b), with a typical diameter between 2 and 3 μm. Images taken at higher magnifications reveal that the microsphere shells are assembled of compactly arranged NTs (Figure 1c and d). A shell thickness of ∼370 nm agrees well with the length of individual NTs (340−390 nm, Figure 2a). NT cavities have a tetragonal shape and can be clearly seen in Figure 1d.

Our microscopy studies (Figures 1 and 2) indicate that the presence of Fe^{3+} ions in a reaction mixture plays a crucial role for the NT formation. When the reaction was carried out under the same conditions but without Fe^{3+} ions in the reaction mixture, MnO$_2$ product was grown in the form of nanorods, regardless of the acid.[25−27] Investigating the influence of Fe^{3+} ions, we also found that the molar ratio between KMnO$_4$ and Fe$_2$(SO$_4$)$_3$ is a key parameter for the NT formation and their self-assembly. In a typical reaction that resulted in 3D microspheres composed of NTs, this ratio was 1:0.15, whereas reducing it to 1:0.075 led to formation of microspheres that were mainly composed of nanorods. When the molar ratio was increased to 1:0.30, NTs were formed, but they did not self-assemble into microspheres.
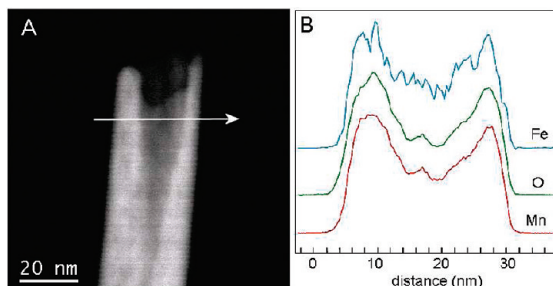
Figure 3. (a) HAADF-STEM image of the end of a NT and (b) chemical profile obtained from the EELS analysis of the Fe L, O K, and Mn L edges along the line shown in panel a. The presence of a cavity is nonambiguous, since all three components have decreased intensities in the center of the tube, which matches with the lower contrasted area of the dark field image.

To grow α-MnO$_2$ NTs, Luo et al[18] used a Si substrate and the same precursor, but without the presence of Fe^{3+} ions. In their case, NTs grew with diameters that exceed 100 nm. Self-assembly of α-MnO$_2$ NTs into micrometer-size microspheres is unusual and hasn't been encountered before. In products synthesized without the presence of Fe^{3+} ions, microspheres of similar dimensions had been observed,[28,29] but the basic building units were nanorods. Therefore, our hydrothermal decomposition of KMnO$_4$ in the presence of Fe^{3+} ions represents a very simple and efficient method for a large-scale synthesis of small-diameter α-MnO$_2$ NTs.

The phase purity and crystal structure parameters of the product grown under hydrothermal conditions by a reduction of KMnO$_4$ in the presence of Fe^{3+} were examined by X-ray diffraction (XRD). All peaks in the XRD pattern of as-prepared material can be indexed with an existing structure of hollandite MnO$_2$-type structure (JCPDS 44 No. 77-1796; see Figure S1 of the Supporting Information).

Next, transmission electron microscopy (TEM) was employed to examine details of the NT structure. The outer diameter of the NTs ranges between 25 and 40 nm and is very uniform along the individual NT. The wall thickness at the NT end is typically around 5 nm. However, the diameter of the inner cavity is not uniform along the NT (Figure 2a), and it gradually reduces from one end to the other. In fact, the inner cavities rarely extend through the entire NT. The shape of the inner cavities is probably a result of preferential coordination assisted dissolution[30] of MnO$_2$. More experimental work is needed to verify this proposal.

The interplanar distances of TEM fringes parallel to the rod axis are 0.5 nm, which agrees well with the *d* value of (200) planes of α-MnO$_2$. Therefore, the direction of NTs growth is along the [001] direction. This observation holds for NTs with a very rough and porous surface (Figure 2b) as well as for those with a smooth and nonetched surface (Figure 2c).

The chemical composition of the NTs was determined with EELS in combination with STEM. EELS mapping (Figure 3a) for O 1s, Mn 2p, and Fe 2p excitations was preformed across the tube diameter where the intensities of these three excitations are plotted across the tube diameter (Figure 3b). The presence of a cavity is nonambiguous, since all three components have decreased intensities in the center of the tube which match with the lower contrasted area of the dark-field image. The Mn and O profiles show a complete correlation, whereas the Fe profile has more fluctuations, which is due to the lower content of iron in the material. Indeed, all chemical maps show that iron atoms are located within the structures (and not at the surface, within the cavity, or as surrounding nanoparticles). After quantification,
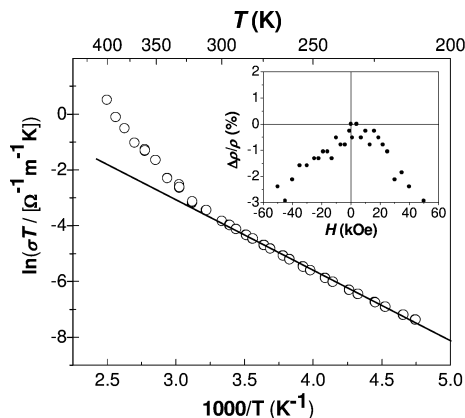

Figure 4. Temperature dependence of electrical conductivity measured on a pressed pellet of MnO$_2$ NTs. The solid line is a fit to a model of adiabatic hopping motion of small polarons (see text for details). Inset: room temperature magnetoresistivity as a function of the applied magnetic field.

the EELS analysis gave a K−Fe−Mn−O atomic ratio of 0.01−0.09−0.58−1 (K$_{0.02}$Fe$_{0.18}$@Mn$_{1.16}$O$_2$), bearing in mind that the typical EELS accuracy of metal−oxygen elemental ratio is below 0.05.

Magnetic and transport properties of MnO$_2$ are governed not only by the crystallographic phase but also by the ratio between Mn^{3+} and Mn^{4+}. With the aim of determining this ratio, we preformed the soft X-ray absorption (SXA) measurements. From comparison between the spectra of MnO$_2$ NTs and reference MnO$_2$ and Mn$_2$O$_3$, it was roughly estimated that at least 93% of the manganese is in an oxidation state of 4+ (for further information, see the Supporting Information, Figure S2), which generally agrees with the above chemical composition.

The Mn^{3+}/Mn^{4+} mixed valence state of the MnO$_2$ NTs prompted us to investigate their electrical transport and magnetic properties. The temperature dependence of electric conductivity (σ) is shown in Figure 4. At room temperature, we estimated the conductivity to be σ (300 K) = 0.02 Ω^{-1} m^{-1} which is roughly an order of magnitude less than it was reported for bulk K$_{1.33}$Mn$_8$O$_{16}$.[31] The temperature dependence of the conductivity is clearly not a metallic type. In addition, we could not find a unique model that would reasonably describe the temperature dependence of σ for the entire temperature range between 400 and 200 K. Namely, a nonlinear dependence of ln σ versus $1/T$ has been measured with a change of slope just around room temperature. A variable range hopping model due to Anderson localization,[32,33] $\sigma(T) = \sigma_0 \exp[-(T_0/T)^{1/(d+1)}]$, was first tested but failed to describe the data above room temperature. Here, T_0 is a characteristic temperature that depends on the density of states at the Fermi level, and $d = 1$ is the dimensionality of the system. This model worked well for the bulk Ba$_{1.2}$Mn$_8$O$_{16}$ compound[34] but much less in our case. Slightly better agreement could be obtained when the conductivity model assumed an adiabatic hopping motion of small e$_g$ polarons[35] with temperature dependence of the form $\sigma(T) \propto 1/T \exp[-E_a/k_BT]$. Taking into account only the 300−200 K temperature interval, good agreement with the data could be achieved with an activation energy E_a/k_B = 2200 K. Apparent problems with the data analysis assuming only a single transport mechanism therefore imply that another parallel conductivity channel, such as fluctuation-induced tunneling,[32] has to be considered, too. In addition, the electrical resistivity of the pressed pellet as a function of the applied magnetic field at room temperature (inset in Figure 4) was measured. A small negative magnetoresistivity,
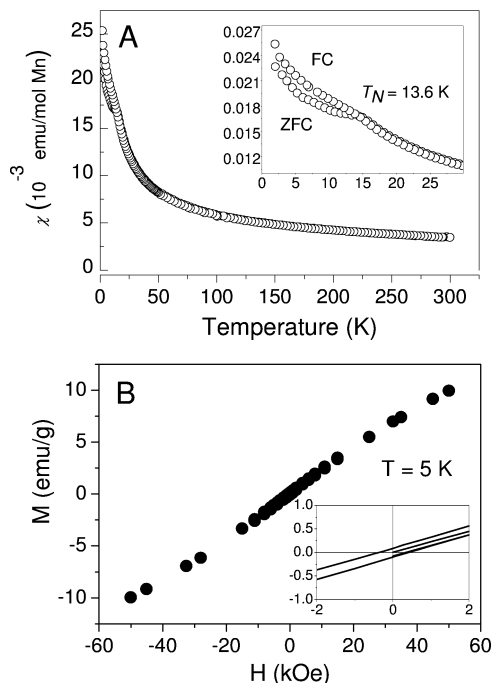
α-MnO₂ Nanotubes

J. Phys. Chem. C, Vol. 113, No. 33, 2009 **14801**

Figure 5. (a) Temperature dependence of dc magnetic susceptibility measured in an applied magnetic field of 100 Oe. Inset: expanded region around the magnetic ordering temperature, $T_N = 13.6$ K, showing the difference between ZFC and FC measurements. The diamagnetic contribution of the sample holder was subtracted from the measured data. (b) Magnetization curve measured at 5 K. Inset: a magnified region showing magnetic hysteresis loop.

with $\Delta\rho/\rho$ being ∼3% for the highest applied magnetic field ($H = 5$ T), was obtained.

The temperature dependence of the magnetic susceptibility (χ) is shown in Figure 5a. Strong Curie-like temperature dependence above 100 K points toward the charge localization and is consistent with the electrical conductivity measurements. However, a large positive offset in χ suggests also a strong paramagnetic temperature-independent contribution possibility arising from the coexisting metallic regions. Analysis of the raw susceptibility data between room temperature and 100 K with a phenomenological model, where χ is composed of the Curie–Weiss and a temperature independent term, χ_0,

$$\chi = \frac{C}{T - \theta} + \chi_0 \qquad (1a)$$

required a reduced Curie constant, $C = 0.9$ emu K/mol Mn (corresponding to an average magnetic moment of only $2.7\mu_B$ per Mn^{3+}/Mn^{4+}) and unexpectedly large paramagnetic $\chi_0 = 1.1 \cdot 10^{-3}$ emu/(mol Mn). Three contributions to χ_0 must be considered[36] (measurements of χ in different magnetic fields rule out the ferromagnetic impurities as a source of the large paramagnetic susceptibility χ_0; see the Supporting Information): (i) the Larmor diamagnetism of core electrons χ_{Larmor}, (ii) the Pauli paramagnetism of conduction electrons χ_{Pauli}, and (iii) the Landau diamagnetism χ_{Landau} due to the orbital electron motion that amounts to $\chi_{Landau} \approx -1/3 \chi_{Pauli}$. Term (i) can be estimated from the Pascal tables[37] and is approximately $\chi_{Larmor} = -1.4 \cdot 10^{-5}$ emu/(mol Mn). Terms (ii) and (iii), which are positive and negative, respectively, are usually of the same order of magnitude as χ_{Larmor}. Thus, the measured $\chi_0 = \chi_{Landau} + \chi_{Pauli} + \chi_{Larmor}$ is at least an order of magnitude larger than expected for ordinary metals within the independent electron approxima-

tion. At this point, we should mention that similar anomalously large Pauli paramagnetism has been already detected in another quasi one-dimensional system; namely, in doped MoS₂ nanotubes.[38]

The above simple model (eq 1) was, however, not completely adequate for describing the susceptibility data over an entire temperature range. After subtraction of χ_0 from the raw data, the inverse corrected susceptibility $1/(\chi - \chi_0)$ follows a straight line with a Curie–Weiss temperature $\theta = -58(5)$ K in accordance with eq 1a. However, a crossover in $1/(\chi - \chi_0)$ is found around ∼250 K (see the Supporting Information, Figure S5). This coincides with the crossover temperature found in the conductivity measurements (Figure 4). The observed anomaly in χ, in fact, reflects the transition from the regime, where hopping of e_g electrons freezes out and the averaged valence state between Mn^{3+} and Mn^{4+} changes to a charge separation with clearly distinguished Mn^{3+} ($S = 2$) and Mn^{4+} ($S = 3/2$) ions. Below ∼70 K, deviations from the linear dependence of $1/(\chi - \chi_0)$ are taken as evidence for the development of short-range order effects which develop into a long-range order at $T_N = 13.6$ K (inset to Figure 5a), where a cusp in the magnetic susceptibility is observed. AC magnetic susceptibility measurements, not shown here, rule out spin glass ground state. This transition temperature is suppressed compared to ordering temperatures reported for bulk Ba$_{1.2}$Mn$_8$O$_{16}$ ($T_C = 40$ K)[34] or K$_{1.5}$(H$_3$O)$_x$Mn$_8$O$_{16}$ (ferromagnetic transition at $T_C = 52$ K).[39] Evidently, nanometric morphology and structural inhomogeneities play against magnetic ordering in α-MnO₂ NTs. In the magnetically ordered phase, a difference between ZFC (zero filed cooled) and FC (filed cooled) measurements is noticed. The magnetization in an applied field of $H = 100$ Oe at 2 K converges to a weak moment of 2.6 emu/(mol Mn). A magnetic hysteresis loop (Figure 5b) with a coercive field of around 400 Oe is measured at $T = 5$ K, but the magnetization still increases, even at the applied magnetic field of $H = 50$ kOe so that the ground state is antiferromagnetic in character, and the observed weak ferromagnetic moment is due to either the mixed valence Mn^{3+}/Mn^{4+} regions or spin canting caused by magnetic anisotropies.

Both bulk conductivity and magnetic susceptibility measurements suggest inhomogeneous and complex behavior of investigated α-MnO₂ NTs. To address the role of such inhomogeneities at the nanoscale, we decided to employ local probe electron paramagnetic resonance (EPR) technique. EPR spectra were successfully fitted with two overlapping Lorentzian components (Figure S4) reflecting the presence of two spatially separated regions in the sample. Both components have similar g-factors, but very different line widths. Between room temperature and ∼150 K, the EPR spin susceptibility χ_{EPR} of a broad component is almost temperature-independent (Figure 6a), as expected for the phase with delocalized e_g electrons. Interestingly, we notice in the same temperature interval a gradual increase of the g-factor from 1.999 to 2.005. Below 150 K, χ_{EPR} starts to gradually increase, whereas the g-factor remains almost temperature-independent. The temperature dependence of the line width is also very interesting. Namely, at high temperatures, the EPR line width decreases with decreasing temperature, reaches a shallow minimum at around 70 K, and then starts to increase again on further cooling toward the Néel temperature (T_N) due to the critical broadening. At high temperatures, $\Delta H_{1/2}$ can be well described (similar to the electrical conductivity (Figure 4)) with activated type temperature dependence: $\Delta H_{1/2} = (A)/(T) \exp[-(E_a)/(kT)]$ (solid line in Figure 6b). A close similarity between the temperature dependences of the EPR line
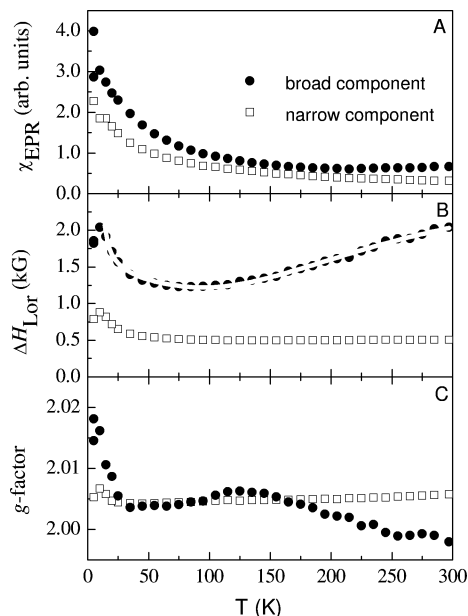
14802 *J. Phys. Chem. C, Vol. 113, No. 33, 2009*

Umek et al.

Figure 6. Temperature dependences for the EPR (a) spin susceptibility, (b) linewidth, and (c) g-factors. In all cases, solid circles stand for the broad and open squares for the narrow EPR components. The solid line in panel b is a fit to the activated type of dependence of the EPR line with an activation energy of $E_a = 1000$ K.

width and the conductivity is often observed in systems with hopping conductivity, such as mixed-valence manganese oxides. In our case, this could appear due to the intercalation of K^+ or incorporation of Fe^{3+} into the structure of hollandite α-MnO_2. In such a situation, the small polaron hopping of the e_g electron from a Jahn−Teller-active Mn^{3+} ($t_{2g}^3 e_g^1$) to a non-active Mn^{4+} ($t_{2g}^3 e_g^0$) site is responsible for the good conduction and the peculiar dependence of the EPR line width.[17] The broad component arises from the region characterized by the mixed-valence Mn^{3+}−Mn^{4+} state. Apparently, the dynamics of hopping crosses the EPR time window between room temperature and 150 K affecting the measured g-factor value.

We now turn to the temperature dependence of the narrow component. In contrast to the broad component, the EPR susceptibility of a narrow component follows the Curie−Weiss dependence for all temperatures. The extracted Curie−Weiss temperature for the narrow component is $\theta = -52(5)$ K; that is, within the experimental accuracy, the same as derived from the susceptibility data. The part of the sample that participates in this signal has therefore localized manganese moments which we associate with Mn^{4+} ($t_{2g}^3 e_g^0$) only. From EPR line shape analysis, this spectral component reflects about ∼40 % of the total sample. The Curie constant determined from the magnetic susceptibility data then corresponds to an effective Mn moment $p_{eff} = 4.14 \mu_B$, which is a value that is close to what is expected for Mn^{4+} ($S = 3/2$) ions. We therefore suggest that the phase responsible for the narrow EPR signal is the phase with the dominant Mn^{4+} contribution; that is, the phase in which the K^+ content is kept rather low.

Very different temperature dependences of the narrow and broad EPR components suggest that the mixed-valence Mn^{3+}/Mn^{4+} and Mn^{4+} regions are spatially separated. This result also agrees with the above bulk conductivity and magnetic susceptibility measurements, which could not be explained with a single-phase model. From the EPR measurements, we suggest that the observed phase segregation depends on the Mn^{3+} content and therefore likely reflects the structural inhomogeneities at

the nanoscale; that is, the variations in the K^+ and Fe^{3+} doping. Such structural inhomogeneities, which are decisive for the magnetic and conducting properties of nanostructures, may be common to most of the manganese oxide nanostructures grown from the hydrothermal techniques and should be taken into account.

Conclusions

In conclusion, we report on a new synthesis pathway for α-MnO_2 NTs doped with K^+ and Fe^{3+} ions and their self-assembly into hollow microstructures. The NT growth requires the presence of Fe^{3+} ions in a reaction mixture and may be adopted also for growth of other MnO_x polymorphs. Microscopy studies reveal highly crystalline nanotubular morphology with outer diameter not exceeding 40 nm and with an average length of ∼370 nm that correspond to the shell thickness of hollow microstructures. Small variations in the chemical composition at the nanoscale level are responsible for the rich temperature dependence of their conductivity and magnetic properties. From the conductivity, magnetic susceptibility, and EPR measurements, the phase segregation into the insulating phase with predominant Mn^{4+} character and highly conducting phase with substantial Mn^{3+} doping is suggested. In the later phase, the small polaron hopping of the e_g electron with an activation energy of $E_a/k_B = 2200$ K determines the conductivity and the EPR line width. In the former phase, a strong antiferromagnetic exchange acts between manganese ions with an effective moment of $p_{eff} = 4.14 \mu_B$. Further investigations on the role of Fe^{3+} and K^+ doping for the magnetic and conducting properties are required to understand the microscopic mechanism of phase segregation. This effect will have to be considered in any future application of α-MnO_2 NT's self-assemblies.

Supporting Information Available: Figures showing the XRD, SXA, magnetic and EPR measurements accompanied by a brief explanation. This material is available free of charge via the Internet at http://pubs.acs.org.

References and Notes

(1) Ding, Y.-S.; Shen, X.-F.; Gomez, S.; Luo, H.; Aindow, M.; Suib, S. L. *Adv. Funct. Mater.* **2006**, *16*, 549.
(2) Manna, L.; Milliron, D. J.; Meisel, A.; Scher, E. C.; Alivisatos, A. P. *Nat. Mater.* **2003**, *2*, 382.
(3) Jun, Y.-w.; Jung, Y.-y.; Cheon, J. *J. Am. Chem. Soc.* **2002**, *124*, 615.
(4) Hu, J.-S.; Zhong, L.-S.; Song, W.-H.; Wan, L.-J. *Adv. Mater.* **2008**, *20*, 2977.
(5) Umek, P.; Cevc, P.; Jesih, A.; Gloter, A.; Ewels, C. P.; Arčon, D. *Chem. Mater.* **2005**, *17*, 5945.
(6) Thackeray, M. M. *Prog. Solid State Chem.* **1997**, *25*, 1.
(7) Thackery, M. M.; David, W. I. F.; Bruce, P. G.; Goodenough, J. B. *Mater. Res. Bull.* **1983**, *18*, 461.
(8) Armstrong, A. R.; Bruce, P. G. *Nature* **1996**, *381*, 499.
(9) Shen, Y. F.; Zerger, R. P.; DeGuzman, R. N.; Suib, S. L.; McCurdy, L.; Potter, D. I.; O'Young, C. L. *Science* **1993**, *260*, 511.
(10) Liang, S.; Teng, F.; Bulgan, G.; Zong, R.; Zhu, Y. *J. Phys. Chem. C* **2008**, *112*, 5307.
(11) Morimoto, Y.; Asamitsu, A.; Kuwahara, H.; Tokura, Y. *Nature* **1996**, *380*, 141.
(12) Devaraj, S.; Munichandraiah, N. *J. Phys. Chem. C* **2008**, *112*, 4406.
(13) Ma, R.; Bando, Y.; Zhang, L.; Sasaki, T. *Adv. Mater.* **2004**, *16*, 918.

α-MnO$_2$ Nanotubes

J. Phys. Chem. C, Vol. 113, No. 33, 2009 **14803**

(14) Cheng, F.; Zhao, J.; Song, W.; Li, C.; Ma, H.; Chen, J.; Shen, P. *Inorg. Chem.* **2006**, *45*, 2038.

(15) Fei, J.; Cui, Y.; Yan, X.; Qi, W.; Yang, Y.; Wang, K.; He, Q.; Li, J. *Adv. Mater.* **2008**, *20*, 452.

(16) Wang, N.; Cao, X.; He, L.; Zhang, W.; Guo, L.; Chen, C.; Wang, R.; Yang, S. *J. Phys. Chem. C* **2008**, *112*, 365.

(17) Shen, X.-F.; Ding, Y.-S.; Liu, J.; Cai, J.; Laubernds, K.; Zerger, R. P.; Vasiliev, A.; Aindow, M.; Suib, S. S. *Adv. Mater.* **2005**, *17*, 805.

(18) Luo, J.; Zhu, H. T.; Fan, H. M.; Linag, J. K.; Shi, H. L.; Rao, G. H.; Li, J. B.; Du, Z. M.; Shen, Z. X. *J. Phys. Chem. C* **2008**, *112*, 12594.

(19) Zheng, D.; Sun, S.; Fan, W.; Yu, H.; Fan, C.; Cao, G.; Yin, Z.; Song, X. *J. Phys. Chem. B* **2005**, *109*, 16439.

(20) Wang, X.; Li, Y. *Chem.—Eur. J.* **2003**, *9*, 300.

(21) Wu, M.-S.; Lee, J.-T.; Wang, Y.-Y.; Wan, C.-C. *J. Phys. Chem. B* **2004**, *108*, 16331.

(22) Ma, R.; Bando, Y.; Sasaki, T. *J. Phys. Chem. B* **2004**, *108*, 2115.

(23) Kawai, J.; Mizutani, Y.; Sugimura, T.; Sai, M.; Higuchi, T.; Harada, Y.; Ishiwata, Y.; Fokushima, A.; Fujisawa, M.; Watanabe, M.; Maeda, K.; Shin, S.; Gohshi, Y. *Spectrochim. Acta, Part B* **2000**, *55*, 1385.

(24) Cotton F. A.; Wilkinson G., *Advanced Inorganic Chemistry*; Interscience Publishers, John Wiley & Sons: New York, 1962, p 700.

(25) Wang, H.; Lu, Z.; Quian, D.; Li, Y.; Zhang, W. *Nanotechnology* **2007**, *18*, 115616.

(26) Chen, X.; Li, X.; Jiang, Y.; Shi, C.; Li, X. *Solid State Commun.* **2005**, *136*, 94.

(27) Wang, H.; Qian, D.; Lu, Z.; Li, Y.; Cheng, R.; Zhang, W. *J. Cryst. Growth.* 2007. doi:10.1016/jcrysgro.2007.01.034.

(28) Li, B.; Rong, G.; Xie, Y.; Huang, L.; Feng, C. *Inorg. Chem.* **2006**, *45*, 6404.

(29) Li, Z.; Ding, Y.; Xiong, Y.; Yang, Q.; Xie, Y. *Chem. Commun.* **2005**, 918.

(30) Jia, C.-J.; Sun, L.-D.; Yan, Z.-G.; You, L.-P.; Luo, F.; Han, X.-D.; Pang, Y.-C.; Zhang, Z.; Yan, C.-H. *Angew. Chem., Int. Ed.* **2005**, *44*, 4328.

(31) Vicat, J.; Fanchon, E.; Strobel, P.; Tran Qui, D. *Acta Crystallogr. B* **1986**, *42*, 162.

(32) Taguchi, H.; Sonoda, M.; Nagao, M. *J. Solid State Chem.* **1998**, *137*, 82.

(33) Filipič, C.; Levstik, A.; Kutnjak, Z.; Umek, P.; Arčon, D. *J. Appl. Phys.* **2007**, *101*, 084308.

(34) Ishiwata, S.; Bos, J. W. G.; Huang, Q.; Cava, R. J. *J. Phys. Condens. Mater.* **2006**, *18*, 3745.

(35) Shengelaya, A.; Zhao, G.-m.; Keller, H.; Müller, K. A.; Kochelaev, B. I. *Phys. Rev. B* **2000**, *61*, 5888.

(36) Ashcroft, N. W.; Mermin, N. D. *Solid State Physics*, Saunders College Publishing, 1976, pp 657−658.

(37) Dutta, R. L.; Syamal, A. *Elements of Magnetochemistry*, Affiliated East-West Press PVT LTD, 1993, p 8.

(38) Mihailović, D.; Jagličić, Z.; Arčon, D.; Mrzel, A.; Zorko, A.; Remškar, M.; Kabanov, V. V.; Dominko, R.; Gaberšček, M.; Gómez-García, C. J.; Martínez-Agudo, J. M.; Coronado, E. *Phys. Rev. Lett.* **2003**, *90*, 146401.

(39) Sato, H.; Enoki, T.; Yamaura, J.-I.; Yamamoto, N. *Phys. Rev. B* **1999**, *59*, 12836.